SEE CORRECTION FOR THIS ARTICLE
PNAS RESEARCH ARTICLE | ENVIRONMENTAL SCIENCES

How spatiotemporal dynamics can enhance ecosystem resilience

Pablo Moreno-Spiegelberg[a], Max Rietkerk[b], and Damià Gomila[a,1]

Edited by Pablo Marquet, Pontificia Universidad Catolica de Chile, Santiago, Chile; received June 21, 2024; accepted February 11, 2025

We study how self-organization in systems showing complex spatiotemporal dynamics can increase ecosystem resilience. We consider a general simple model that includes positive feedback as well as negative feedback mediated by an inhibitor. We apply this model to *Posidonia oceanica* meadows, where positive and negative feedbacks are well documented, and there is empirical evidence of the role of sulfide accumulation, toxic for the plant, in driving complex spatiotemporal dynamics. We describe a progressive transition from homogeneous meadows to extinction through dynamical regimes that allow the ecosystem to avoid the typical ecological tipping points of homogeneous vegetation covers. A predictable sequence of distinct dynamical regimes is observed as mortality is continuously increased: turbulent regimes, formation of spirals and wave trains, and isolated traveling pulses or expanding rings, the latter being a harbinger of ecosystem collapse, however far beyond the tipping point of the homogeneous cover. The model used in this paper is general, and the results can be applied to other plant–soil spatially extended systems, regardless of the mechanisms behind negative and positive feedbacks.

resilience | plant–soil interactions | excitability | vegetation patterns | traveling pulses

Significance

In hard environmental conditions, vegetation self-organizes forming heterogeneous landscapes that increase ecosystem resilience. So far, this has been studied in vegetation with scale-dependent feedbacks leading to stationary patterns. In this paper, we study plant species that accumulate toxins in the soil, generating complex spatiotemporal landscapes, as in *Posidonia oceanica*. This plant organizes in traveling patterns where the toxin–plant interaction is globally reduced, allowing the ecosystem to survive under adverse conditions. The patterns follow a predictable sequence as mortality increases, matching aerial images of *P. oceanica*. Our results can predict regime shifts due to climate change and apply to a whole family of ecosystems with plant–soil interactions.

Spatial self-organization serves as a resilience mechanism enhancing positive feedbacks over negative feedbacks to enable ecosystems to persist even under adverse conditions (1, 2). This phenomenon has often been studied in semiarid ecosystems that exhibit stationary patterns or patterns that move along slopes (3–5), but much less is known about systems presenting persistent self-sustained oscillations and excitable dynamics, as observed, for example, in seagrass meadows (6, 7), soil fungus (8), high-altitude wetlands (9) and salt marshes (10).

Excitable systems are characterized by having a linearly stable rest state that, when subject to perturbations above a critical threshold, undergoes a large, transient excursion through phase space before returning to the rest state. When extended in space, this sensitivity to perturbations makes excitable media exhibit rich spatiotemporal behaviors. Unlike static Turing patterns, which result from finite wavelength linear instabilities, excitable media can generate a wide variety of dynamic spatial structures in response to local perturbations. These structures include expanding rings, moving wavefronts, spirals, and isolated traveling pulses (11–14).

Excitable media are ubiquitous across different branches of physics and biology. They are critical in understanding signal propagation in neuroscience, where excitable dynamics underlie neural firing and the propagation of action potentials in axons (15, 16). In cardiac tissue, excitable behavior governs the heart's electrical activity, with abnormal patterns like spirals associated with life-threatening arrhythmias (14, 17). Excitable behavior also manifests in chemical reaction–diffusion systems, with well-known examples like the Belousov–Zhabotinsky reaction, where chemical waves and self-replicating spots have been observed experimentally (11, 12, 18). Moreover, excitable systems are relevant in photonics, where nonlinear optical cavities can exhibit several excitable behaviors (19, 20).

Excitability has recently gained significant attention in ecology, particularly in the study of complex spatiotemporal patterns in vegetation. In ecosystems, feedback mechanisms between vegetation and the environment, such as resource availability or the accumulation of toxins, can create conditions analogous to those in excitable media. Localized disturbances in these systems can trigger vegetation to propagate as traveling waves, spirals, or pulses, akin to the behavior observed in physical excitable systems. This framework helps explain the resilience and collapse of ecosystems under environmental stress, providing insights into vegetation dynamics. In particular, these systems appear to align with what is known as Type-I excitability. This type of excitability does not require large differences in time scales between system variables and allows excitable trajectories toward the unpopulated solution without exhibiting negative population densities. More details on excitability types are included in *SI Appendix*, Text.

Author affiliations: [a]Institute for Cross-Disciplinary Physics and Complex Systems (Consejo Superior de Investigaciones Científicas - Universitat de les Illes Balears), Palma de Mallorca E-07122, Spain; and [b]Copernicus Institute of Sustainable Development, Section Environmental Sciences, Utrecht University, Utrecht 3508 TC, The Netherlands

Author contributions: P.M.-S., M.R., and D.G. designed research; P.M.-S. and D.G. performed research; P.M.-S. analyzed data; and P.M.-S., M.R., and D.G. wrote the paper.

The authors declare no competing interest.

This article is a PNAS Direct Submission.

[1]To whom correspondence may be addressed. Email: damia@ifisc.uib-csic.es.

This article contains supporting information online at https://www.pnas.org/lookup/suppl/doi:10.1073/pnas.2412522122/-/DCSupplemental.

Published March 13, 2025.

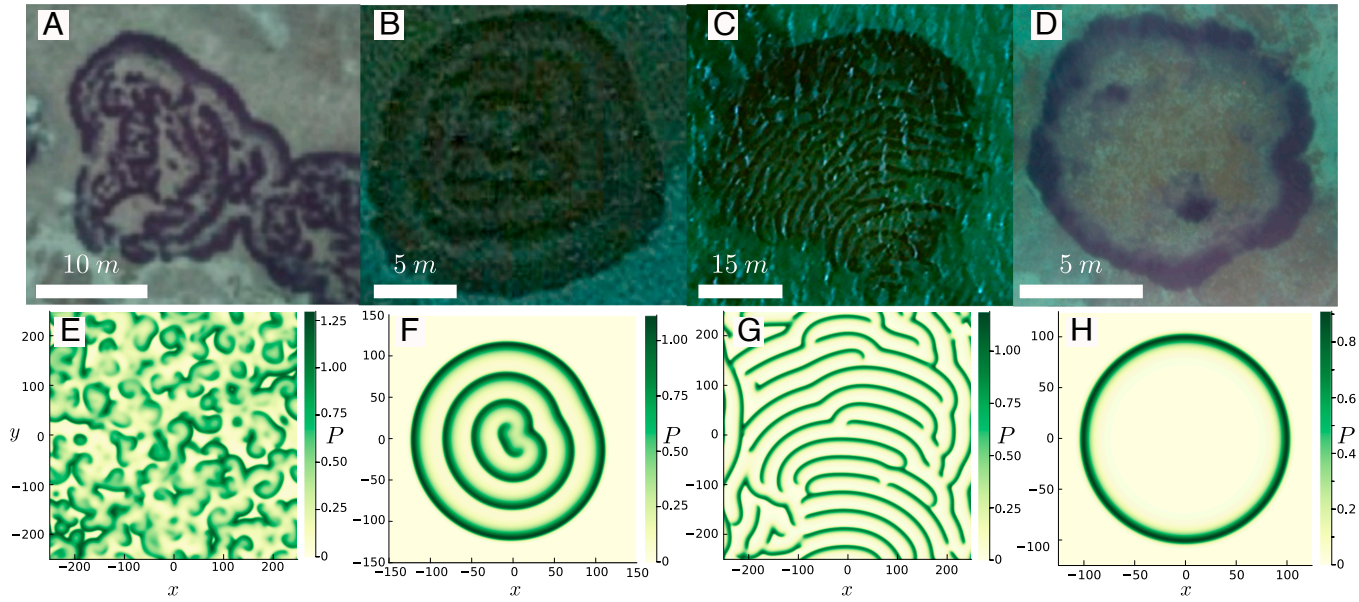

Fig. 1. Comparison of aerial images of *P. oceanica* patterns (*A*–*D*) with numerical simulations of Eq. **1** (*E*–*H*). From *Left* to *Right*: turbulent regime, target pattern formed by two counterrotating spirals, wave trains, and expanding ring. Simulations are performed for (*E*) $\omega = -0.0016$, (*F*) $\omega = 0.0016$, (*G*) $\omega = 0.08$, and (*H*) $\omega = 0.096$. Other parameters: $\alpha = 1.6$, $\tau = 6.25$. Simulation (*F*) is obtained from initial radial Gaussian plant and toxin distributions. The centers of the initial Gaussians are shifted, breaking the rotational symmetry. The formation process of this structure, as well as aerial images of target patterns in different stages of development, are included in *SI Appendix*. Simulation (*H*) is obtained from an initial radial Gaussian plant distribution. Simulations (*E* and *G*) are snapshots of Fig. 3 at the corresponding value of ω. Panels (*A* and *D*) are taken from high-resolution drone images at (39° 53′ 45, 1″*N*, 3° 04′ 54, 3″*E*) and (39° 53′ 53, 0″*N*, 3° 04′ 55, 0″*E*). Panels (*B* and *C*) are taken from Google Earth at (39° 54′ 18, 0″*N*, 3° 06′ 20, 2″*E*) and (32° 12′ 8, 6″*N*, 23° 16′ 42, 5″*E*). Movies showing simulations (*E*–*H*) can be found in Movies S3, S6, S8, and S9 respectively).

For example, the formation of vegetation rings has been attributed to mechanisms such as water competition (21–25), morpho-phenological factors (26), aeolian processes (25, 27), and plant–soil feedbacks (28–31). The latter suggests that the formation of these structures is driven by a negative feedback mediated by an inhibitor, such as a harmful toxin or allelopathic substance produced by the plants themselves. These substances concentrate in the soil, increasing the mortality rate within the population. A paradigmatic example is found in seagrass meadows (6, 7, 32), where the decomposition of organic matter into toxic sulfide compounds acts as the inhibitor, promoting the formation of rings and other spatiotemporal structures (6, 7, 33–37).

Similar mechanisms have been studied in other plant species (9, 10, 38–43) and fungal systems (8, 44, 45). Applying the concept of excitable behavior from physics to these ecological systems provides a powerful tool to understand the complex dynamics of vegetation, offering a broader perspective on the processes that shape these ecosystems and the critical transitions they may undergo under varying environmental conditions.

In this work, we study the transition from a homogeneous vegetation cover to extinction as the mortality rate increases in systems showing such complex spatiotemporal dynamics. We use a prototypical model that includes positive feedback and a negative feedback mediated by an inhibitor applicable to a wide range of ecosystems, going from seagrasses and (not necessarily water-deprived) terrestrial plants, to fungal colonies. The emergent complex spatiotemporal structures enhance the resilience of the ecosystem in that these dynamical structures persist for mortality rates beyond those for which the ecosystem can support a homogeneous vegetation cover.

The typical scenario, illustrated in Fig. 1 with model simulations and aerial images of *Posidonia oceanica* at different locations, is as follows: For low mortality rates, the vegetation cover is uniform (not shown); Increasing the stress on the system, the stationary homogeneous solution destabilizes to oscillations. However, coherent oscillations, uniform or in the form of traveling waves, are unstable and lead to a spatiotemporally disordered state known as defect turbulence in the context of the complex Ginzburg–Landau equation (CGLE)* (47) (Fig. 1 *A* and *E*). When the mortality rate is increased further, coherent oscillations in the form of spirals (Fig. 1 *B* and *F*) or periodic trains of pulses (Fig. 1 *C* and *G*) form out of the turbulent states, leading to more or less regular spatial structures. Multiple solutions with different wavelengths coexist in this regime, and the observed characteristic wavelength increases with stress. Eventually, only isolated traveling pulses of vegetation, which can form expanding rings in 2D (Fig. 1 *D* and *H*), survive until the complete collapse of the vegetation is observed beyond the ultimate tipping point. While this sequence reflects the dynamics of the theoretical model when the mortality rate increases, other environmental factors could differ between different locations, partially influencing the observed patterns. However, the general sequence of patterns is robust to parameter changes.

1. Model

To address this problem, we introduce a minimal model that captures the essential mechanisms driving the formation of traveling pulses, which represent the key resilient spatial structures in the ecosystem. This model is based on two interacting fields: $P(x, y, t)$, which represents the density of plant population, and $T(x, y, t)$, which represents the concentration of toxins in the sediment. The dynamics of these two fields are governed by a

*In the CGLE, which describes the general spatiotemporal dynamics of spatial systems close to an oscillatory onset, "turbulence" does not imply the same phenomenon as in classical fluid dynamics, where it is associated with the transfer of energy across scales or power-law scaling in spectral densities. Rather, in the CGLE framework, turbulence typically refers to disordered, aperiodic, and incoherent (chaotic) spatiotemporal behavior (46).

system of partial differential equations describing the feedback between plant growth and toxin accumulation:

$$\partial_t P = (-\omega + \alpha P - P^2 - T)P + \nabla^2 P,$$
$$\tau \partial_t T = P - T + D_T \nabla^2 T. \quad [1]$$

The parameters are defined as follows: ω is the net mortality rate, representing the balance between growth and mortality in the absence of other plants or toxins. This parameter can be influenced by environmental factors such as nutrient availability, light, or temperature; α is the ratio between positive and negative feedback, capturing the plant's growth enhancement in response to increased local density; τ is the timescale for toxin accumulation and decay, reflecting the relative speed at which toxins are produced by plants and removed from the environment as compared to the plant growth timescale; and D_T is the ration between the diffusion coefficient of the toxin and the diffusion coefficient of the plant, that has been normalized to one (*SI Appendix*, Text). ∇^2 is the Laplacian operator that describes the spatial diffusion of both plant density and toxin concentration in sediment.

The first equation describes the local growth of the plant population and its spread throughout the landscape due to spatial diffusion. The model incorporates positive feedback, which is considered to operate much faster than population dynamics. This rapid feedback is effectively modeled as a positive contribution to the total growth rate proportional to population density. As a result, the total (density-dependent) growth rate increases with population density at moderate values of P (due to αP), where positive feedback dominates.

However, as the population density increases and approaches the carrying capacity of the system, the term $-P^2$ takes over, causing the growth rate to saturate. This interplay between positive feedback and carrying capacity creates a nonmonotonic density dependence on the total growth rate, a phenomenon known as the Allee effect. In essence, at low densities, populations benefit from positive feedback, but beyond a certain threshold, resource competition limits further growth.

In addition to growth saturation, the equation for population density also includes the negative impact of the toxin on plants, represented by the term $-T$. The coefficients of these two feedback terms, P^2 and T, have been normalized to one for simplicity, as their relative values can be absorbed into other parameters without loss of generality (see *SI Appendix*, Text for more details).

The equation for toxin concentration T is governed by two key processes: toxin production, which we model as proportional to the plant biomass density P, and toxin degradation, represented by the term $-T$. Both the production and degradation rates are normalized to one, defining the characteristic timescale of toxin dynamics through the parameter τ, which we treat as a critical control variable in our model. While nonlinear terms could be justified in the toxin equation, especially given the complexity of biological and chemical processes in real ecosystems, we adopt a linear form to capture the core dynamics in a straightforward manner. This allows us to focus on the general mechanism of toxin-mediated feedback without unnecessary complexity. Additionally, we assume no diffusion for the toxin ($D_T = 0$), meaning toxins remain localized to areas where plants grow, which is a reasonable approximation for substances confined to the soil. Including toxin diffusion does not qualitatively change the results as long as the toxin diffuses more slowly than the plants (i.e., for small values of D_T).

Together, these equations capture the interaction between the plants and their environment, particularly the inhibitory effects of toxins on plant growth, which are crucial for the formation of traveling pulses. The Allee effect in the plant dynamics and the negative feedback loop between plant density and toxins allow for complex spatiotemporal structures, including traveling pulses, spiral waves, and expanding rings, which are characteristic of excitable media (Fig. 1).

Throughout this study, we fix $\alpha = 1.6$ and $\tau = 6.25$, values that are realistic for *P. oceanica* (see *SI Appendix*, Text for parameter justification), and focus on exploring how changes in ω drive the system through various dynamical regimes. By adjusting ω, we can simulate transitions between homogeneous vegetation states, complex dynamics, and collapse, providing insights into the resilience of ecosystems under different environmental stressors.

2. Model Analysis

In this section, we analyze the formation of spatiotemporal resilient structures governed by Eq. **1**, introducing the essential mechanisms driving these patterns—positive feedback, mediated negative feedback, and plant diffusion—step by step. These elements together form the basis for understanding the complex dynamics of the system. Subsequently, in Section 3, we will build on the dynamical regimes explored here to illustrate the resilience of an ecosystem described by this model in the context of global change, where increasing mortality over time plays a central role.

2.1. Positive Feedback. Here, we consider the case $\tau \to 0$, which corresponds to the limit where the negative feedback from toxins acts instantaneously. In this scenario, the equation for toxin dynamics can be eliminated adiabatically, simplifying the system so that both positive and negative feedback depend solely on plant density. Biologically, this represents a situation in which the toxin concentrations adjust so rapidly after changes in population density that their transient effects can be neglected. As a result, the interaction between plants due to toxins can be interpreted as a direct negative feedback. In this limit, Eq. **1** simplifies to

$$\partial_t P = (-\omega + (\alpha - 1)P - P^2)P + \nabla^2 P, \quad [2]$$

where the term $(\alpha - 1)P$ captures the combined effects of the positive and the negative feedback. It is important to note that for the parameters relevant to *P. oceanica* the positive feedback dominates the negative feedback due to toxins ($\alpha > 1$), making this term positive. Effectively, this means that we are considering a system where positive feedback plays the primary role in driving the dynamics for moderate plant densities.

Despite this simplification, Eq. **2** retains some of the essential features needed for the formation of spatial structures in the original system. Specifically, homogeneous steady states are the same as those considering the toxin dynamics. This is because, in these solutions, the toxin concentration is constant, and the value of τ, which governs the toxin rate of change, becomes irrelevant.

In addition to the trivial (bare) homogeneous steady state $S_0 = (P_0, T_0) = (0, 0)$, Eq. **1** admits two nontrivial (populated) homogeneous steady states

$$S_\pm = (P_\pm, T_\pm) = \frac{(\alpha - 1) \pm \sqrt{(\alpha - 1)^2 - 4\omega}}{2}(1, 1), \quad [3]$$

shown as green curves in the bifurcation diagram of Fig. 2*A*. Since P is a plant density, only positive values are physically

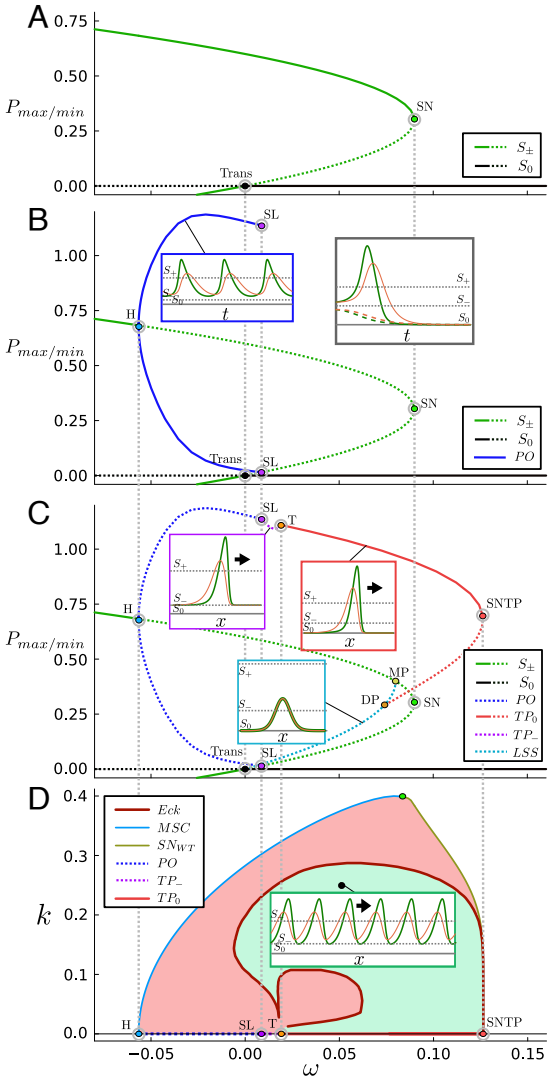

Fig. 2. Bifurcation diagrams of Eq. **1**. (*A*–*C*) Maximum plant density of different spatiotemporal solutions as a function of the mortality rate ω. In (*A*) only solutions of the system without space (temporal system) are shown for $\tau = 0$, corresponding to the case of a system with direct negative feedback. Green lines correspond to steady populated solutions ($S_\pm$) and black lines to the bare state (S_0). Stable (unstable) solutions are represented by solid (dashed) lines. Labeled dots indicate bifurcation points explained in the text. Panel (*B*) extends to solutions with $\tau \neq 0$. In this case, the noninstantaneous negative feedback mediated by toxins destabilizes S_+ to homogeneous temporal oscillations (*PO*). The solid blue line corresponds to the extreme values of the limit cycle. *Insets* show the temporal evolution of plant density and toxin concentration in the oscillatory (blue) and excitable (gray) regimes. Panel (*C*) shows the bifurcation diagram of the full spatiotemporal system and, in addition to the solutions of the temporal system (homogeneous solutions), it includes traveling pulses on S_- (*TP*$_-$, purple lines), traveling pulses on S_0 (*TP*$_0$, red lines), and localized steady states on S_0 (*LSS*, light blue lines). Notice that considering space, *PO* are unstable. *Insets* in panel (*C*) show the spatial profiles of *TP*$_-$ (purple), *TP*$_0$ (red), and *LSS* (light blue). Panel (*D*) shows the phase diagram of wave trains. Depending on the mortality rate ω, wave trains with wavenumber k are stable (unstable) within the green (red) shaded area. The existence region of wave trains is limited on the *Left* by the marginal stability curve (MSC, light blue curve) where small amplitude wave trains emerge from S_+ and limited on the *Right* by a fold of wave trains (green curve). The stability region (green shade) is delimited by an Eckhaus instability (*Eck*, dark red curve). Solutions with $k = 0$ are marked with color lines corresponding to those shown in panel (*A*). Note how $k = 0$ solutions can be homogeneous oscillatory solutions (*PO*, dark blue line) or traveling pulses (*TP*$_-$, purple line, and *TP*$_0$, red line). The transitions between these $k = 0$ solutions correspond to the bifurcations shown in panel (*C*), indicated by vertical dotted gray lines. The *Inset* in panel (*D*) shows the profile of a wave train with $k = 0.25$ for $\omega = 0.046$, marked with a black dot in the panel.

meaningful. The states $S_\pm$ emerge from a saddle-node bifurcation at $\omega_{SN} = 0.09$ (marked as *SN* in Fig. 2*A*) and exist only for $\omega < \omega_{SN}$. For $\tau = 0$ the solution S_+ is stable and the bare state S_0 changes stability in a transcritical bifurcation (black point in Fig. 2*A*) with the solution S_-, which, when positive, is always a saddle.

These two bifurcations divide the parameter space into three regions: for $\omega < 0$ the system exhibits a weak Allee effect, where S_+ is the only stable solution, and any small initial plant density will grow and populate the system. For $0 < \omega < \omega_{SN}$ the model shows a strong Allee effect. In this case, there is a minimum plant density, given by S_-, below which the population collapses. Densities above this threshold grow and stabilize to form a high-density meadow, S_+ (Fig. 2*A*). Finally, for $\omega_{SN} < \omega$, the only stable solution is the bare state S_0 and any initial plant population will decay. Thus, when negative feedback is instantaneous (i.e. $\tau = 0$) the *SN* is the ecological tipping point for which the homogeneous system goes extinct. Furthermore, no resilient spatiotemporal structures form for this system, and no enhanced resilience is possible in the absence of toxin dynamics.

The strong Allee effect observed in the model aligns with empirical evidence in seagrass meadows in restoration attempts (48), tipping points measured along stress gradients (49), and the existence of bistability mechanisms (33, 50–53).

2.2. Noninstantaneous Negative Feedbacks in Homogeneous Systems. When τ is nonzero, the negative effect of population growth is no longer instantaneous, but mediated by the dynamics of the toxin concentration. This leads to a feedback loop in the system. An increase in plant population, driven by positive feedback, increases toxin production with a certain delay, which in turn reduces plant density. The lower plant density then decreases toxin production, allowing the plant population to rise again thanks to the toxin degradation after a certain time.

This feedback loop can destabilize S_+ to oscillations through a Hopf instability (blue dot in Fig. 2*B*), leading to stable periodic oscillations (*PO*) of plant density and toxin concentration (see the blue *Inset* in Fig. 2*B*), i.e. a limit cycle. The dark blue curve in Fig. 2*B* represents the extreme values of the plant density of this cycle. Increasing ω, the amplitude of the cycle increases until it reaches S_-, i.e. the critical plant density of the strong Allee effect, at its minimum. Once this threshold is reached the positive density-dependent feedbacks are too weak for the population to grow and the *PO* is destroyed in a saddle-loop bifurcation (a.k.a. homoclinic bifurcation) for $\omega_{SL} = 0.009$, marked as *SL* (purple dot) in Fig. 2*B*.

For values of ω above ω_{SL}, the only stable solution of the nonspatial system is bare soil, and the system exhibits excitable behavior (see the gray *Inset* in Fig. 2*B*). In this regime a small perturbation to the bare state decays, due to the strong Allee effect (shown as dashed lines in the *Inset*). However, a large enough perturbation, exceeding a certain threshold (in this case the stable manifold of S_-) will grow driven by the positive feedback, reaching a peak and, eventually, decaying back to the bare solution due to toxin accumulation. One of these excitable trajectories is shown with solid lines in the gray *Inset* in Fig. 2*B*. Notice that initially, the plant density (in green) increases faster than the toxin concentration (in orange). Eventually, the plant density reaches a maximum, but due to the high toxin concentration, it begins to decline. The toxin concentration also starts to decrease, with some delay, but this decline is too slow for the plants to recover.

Paradoxically, increasing the timescale of negative feedback (by raising τ) reduces the resilience of the system in the absence of spatial dynamics. In this case, the excitable dynamics lead to inevitable collapse, shifting the ecological tipping point, from a saddle-node (*SN*) bifurcation (as seen for $\tau \to 0$) to a saddle-loop (*SL*) bifurcation, which occurs at lower mortality rates. This shift exemplifies the *enrichment paradox* (54), where changes that appear to improve system viability actually destabilize it.

However, when spatiotemporal dynamics are introduced, self-organizing processes emerge. Plants spread into areas with lower toxin concentrations, continuously colonizing new regions while leaving behind sparsely populated or barren zones with higher toxin levels. This spatial redistribution enables the ecosystem to achieve higher productivity compared to a homogeneous system. It also allows the ecosystem to maintain high biomass levels, even in situations where a nonspatial system would collapse beyond both the *SL* and *SN* thresholds showing enhanced resilience, as will be discussed in Section 3.

2.3. Spatiotemporal Dynamics in the Full System. Before introducing the role of spatiotemporal dynamics in our system, it is essential to emphasize key distinctions between our model and others that also involve space in the formation of resilient structures. In many traditional models, stationary patterns in vegetation arise through a finite-wavelength instability, commonly known as a Turing instability. In plant-toxin activator–inhibitor systems, this mechanism typically occurs when the inhibitor (toxin) diffuses faster than the activator (plant density). In these models, resilience is achieved through static population clusters that maximize the benefits of (short-range) positive feedback while minimizing the negative impact of (large-range) toxins diffusing from neighboring clusters.

In contrast, in our model, where toxins are fixed in the substrate-such as sulfides deposited during dead seagrass decomposition, soil-borne diseases, or allelopathy processes—the diffusion rate of the toxins is expected to be slower than that of plants. As a result, the conditions for generating stationary patterns via the Turing mechanism are not met. Nevertheless, our model allows for the emergence of other spatiotemporal structures, such as defect turbulence, and typical spatial structures of excitable media, including spirals, wave trains, and traveling pulses. These structures are dynamic and nonstationary, driven by the plant's capacity to spread into areas with low toxin concentrations, creating resilience through movement rather than static patterns.

2.3.1. Wave trains. When increasing ω above the Hopf bifurcation, a family of wave trains emerges (47, 55) (see the red and green shaded regions in Fig. 2*D*). A wave train is a periodic solution of the system that propagates in space with fixed velocity and without changing its shape. An example of such a solution is shown in the *Inset* in Fig. 2*D*. In natural meadows, these structures will be seen as periodic stripes that drift over time (Fig. 1*C*). Coexisting wave trains can be characterized by their wavenumber $k = \frac{2\pi}{\lambda}$, where λ is the wavelength, the spatial period of the wave. Then, wave trains with a small value of k will have larger distances between consecutive peaks than wave trains with a higher value of k.

The first wave train to emerge from the Hopf bifurcation is the one with $k = 0$, corresponding to homogeneous *PO* (47, 55). Even if *PO* are stable in the system without space, a weakly nonlinear analysis of the solutions emerging from the Hopf bifurcation (included in *SI Appendix*, Text) shows that *PO* are unstable under nonhomogeneous perturbations (blue dashed line in Fig. 2*C*). Wave trains with finite k values emerge from S_+ for larger values of ω, at the marginal stability curve (*MSC*), shown as a light blue line in Fig. 2*D*, and, as the homogeneous *PO*, are all unstable once created. Wave trains within a certain range of wavenumbers k stabilize for larger values of ω through an Eckhaus instability (*Eck*). The *Eck* instability curve, shown in brown in Fig. 2*D*, is the boundary between unstable (red-shaded region) and stable (green-shaded region) wave trains. Therefore, the shaded green area in Fig. 2*D* is the Busse balloon of coexisting stable wave trains for each value of ω (2, 56). Our analysis also shows that wave trains do not display transverse instabilities, however, they can destabilize in other ways depending on their wavenumber (2, 5, 57, 58) (see the stability analysis of wave trains in *SI Appendix*, Text).

Wave trains with $k \to 0$ can have two very different shapes: almost homogeneous oscillations for values of ω close to the Hopf, the limit cycle (*PO*) already discussed and represented as dark blue curves in Figs. 2 *B* and *C*, or isolated traveling pulses (*TP*), to be discussed in Section 2.3.3, for values of ω beyond the T-point.

2.3.2. Defect turbulence. For values of ω where there are neither stable wave trains nor stable homogeneous steady states, the system exhibits defect turbulence (Fig. 1*E*) (47). Defect turbulence refers to a dynamically disordered state in which the spatiotemporal dynamics of a field is continually disrupted by the formation and annihilation of localized defects in pairs. These defects are points within the oscillatory field where, as one moves around the defect, the phase of the oscillation completes a full 2π cycle. Consequently, the phase becomes undefined at the core of the defect and the oscillation amplitude drops to zero at that point.

This dynamical regime is generic for systems near but above the oscillatory threshold, as described by the Complex Ginzburg–Landau Equation (CGLE), which governs the amplitude of oscillations near a Hopf instability. We have derived the CGLE corresponding to Eq. **1** near the Hopf bifurcation and found that, for the parameters used in this study, the system falls squarely within the defect turbulence region of the CGLE phase diagram (47) (the full derivation is available in *SI Appendix*, Text). This rigorously confirms that the regime shown in Fig. 1*E* corresponds to defect turbulence. Furthermore, this dynamical regime is induced by the Eckhaus instability of wave trains, when reducing the mortality (59).

Close to the Hopf bifurcation, where oscillation amplitudes around the stable state S_+ are small, identifying defects visually can be challenging. In *SI Appendix*, Text, we provide a simulation in this parameter region that explicitly highlights the presence of defects. At mortality rates further above the Hopf bifurcation, where spatial oscillations have larger amplitudes, defects may be observable in natural meadows as the tips of vegetation stripes (such as those in Fig. 1*A*). These defects persist in regions with stable wave trains, as shown in Fig. 1 *C* and *G*. Spirals like the ones shown in Fig. 1 *B* and *F* are also the result of the dynamics driven by the defect at their center. Defect turbulence might underlie the formation of disordered patterns such as the one in Fig. 1*A*. A detailed analysis of defect formation and their number across different dynamical regimes is presented in *SI Appendix*, Text.

2.3.3. Traveling pulses. Traveling pulses (*TP*) are localized structures traveling on a homogeneous steady state. In our system, we find traveling pulses on S_- (TP_-) and traveling pulses on S_0 (TP_0).

Traveling pulses on S_- (TP_-) emerge from the point *SL* (see the dotted purple line in Fig. 2 *C* and *D*) (60). A representative profile of this structure is shown in the purple *Inset* of Fig. 2*C*. These pulses are unstable, as they rest on the

unstable homogeneous state S_- and their branch ends at a T-point bifurcation for $\omega = 0.019$ (60–63) (orange dot in Fig. 2 *C* and *D*). From this T-point, a branch of new stable pulses on S_0 (TP_0) emerges (solid red curve in Fig. 2 *B*–*D*) (64). A representative profile of this structure is shown in the red *Inset* of Fig. 2*C*. In natural meadows, this structure is seen as an isolated vegetation stripe. The ring shown in Fig. 1*D* can be approximated to this structure.

For values of ω above the T-point, pulse-shaped initial conditions generate TP_0 pulses, which are stable in parameter space until they are destroyed in a fold of pulses for $\omega_{SNTP} = 0.126$ (red dot labeled *SNTP* in Fig. 2 *C* and *D*). Therefore, traveling pulses are stable for values of ω above the tipping point of the homogeneous system, ω_{SL}, and even above ω_{SN}. Although in this region, they coexist with wave trains with higher k, traveling pulses are the most resilient solution in the system, as shown in Fig. 2*D*. Notice that the combination of negative feedback mediated by toxins and positive feedback generates spatial structures that persist beyond the existence region of the homogeneous state, thus increasing the resilience of the system. By continuously moving, these structures partially evade the detrimental effects of toxins, enabling their survival under harsher conditions.

Additional branches of pulses can be identified in the system, including low-amplitude traveling pulses (dotted red curve in Fig. 2*C*) and stationary pulses (light blue dotted curve in Fig. 2*C*). However, these solutions are unstable and do not play a significant role in the dynamics described in this paper. More information about these solutions, along with their associated bifurcations, such as the drift-pitchfork (DP) bifurcation and the Maxwell point (MP), is provided in *SI Appendix*, Text.

Similarly, wave trains with $k > 0$ also end in a Fold of Wave Trains. This fold is represented in Fig. 2*D* as an olive-green line. The TP_0, which corresponds to a wave train with $k = 0$, is the last wave train to cross the fold, corresponding to the *SNTP* in this case, and therefore is the last populated solution to vanish for high mortality rates.

3. Ecological Transition in a Global Change Scenario

The bifurcation diagrams shown in Fig. 2 allow one to understand the natural sequence of dynamical regimes an ecosystem will undergo by a slow sustained increase of the mortality rate, for instance, due to climate change. In the case of *P. oceanica* it is well documented that a sea temperature above 28 °C, an increasingly frequent extreme event, significantly increases the mortality rate of *P. oceanica* (65–67). This ecological transition is further illustrated in Fig. 3.

Starting with a low value of ω, below the Hopf bifurcation, a stable homogeneous meadow is stable. Increasing the mortality rate, this state becomes unstable to oscillations. As just above the Hopf bifurcation, all plane wave solutions are unstable (red region in Fig. 2*D*), the system jumps directly into a defect turbulence state (Fig. 3 *A* and *B*). The turbulent state persists up to $\omega \sim 0$, although its average plant density decreases with the mortality rate. From there on, more or less coinciding with the stabilization of wave trains (edge of the green region in Fig. 2*D*), periodic coherent structures in the form of spirals or wave trains emerge out of the spatiotemporal disorder (Fig. 3*C*).

The first coherent structures observed are spirals close to the tipping point in the homogeneous model, i.e. the *SL*. The spirals appear first with a small radius (Fig. 3*C*), which grows as ω increases (Fig. 3*D*). This scenario is similar to what is observed for spirals in the complex Ginzburg–Landau equation (58). The stability of spirals is directly related to the stability of wave trains, as their arms asymptotically tend to plain waves, but the core provides them extra robustness. Typically, spirals can persist even if their arms (plane waves) are asymptotically unstable because the instability is convective, which determines the maximum radius of the spiral before its outer part breaks down. The more unstable the arms, the smaller the radius. For this reason, spirals are smaller close to the turbulent regime, and become larger as wave train solutions gain more stability (inside the green region).

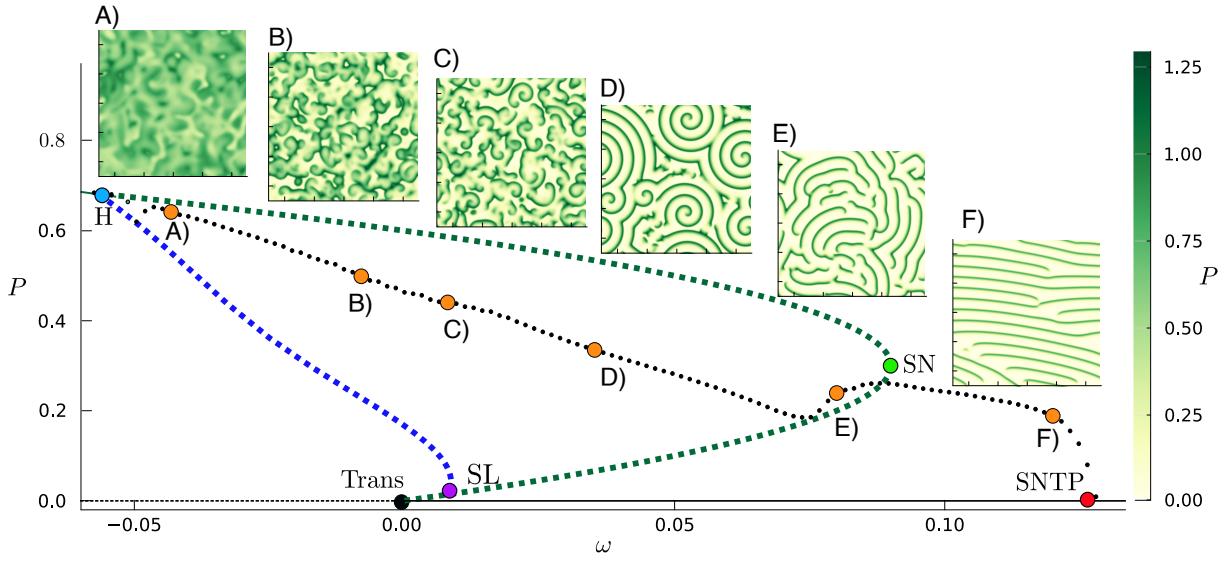

Fig. 3. Mean plant density as a function of ω from a spatially extended simulation with a gradual increase in mortality over time (black dots). The homogeneous populated steady states $S_\pm$ and bare soil S_0 are shown as green and black lines, respectively. The mean plant density of the homogeneous periodic oscillation, *PO*, is represented by a blue dashed line. The stationary and periodic homogeneous solutions correspond to those in Fig. 2*B*. Snapshots of the population density corresponding to the orange points in the plot are shown in *Insets A–F*, illustrating distinct spatiotemporal patterns: turbulent regime (*A–C*), spiral formation around defects (*C* and *D*), and plane-wave trains (*E* and *F*). Relevant bifurcation points are labeled as in Fig. 2*C*. Note how spatiotemporal patterns exhibit a higher biomass density than the homogeneous periodic oscillations (black dots vs. blue dashed line) and persist beyond the tipping point of homogeneous solutions, *SL* and *SN*, indicating enhanced resilience. A fast-forward simulation of the entire transition is available in Movie S1. Movies with detailed temporal resolution of the dynamics in *Insets* (*A–F*) are provided in Movies S2–S7, respectively.

We also observe how the wavelength of the spiral arms increases with ω, decreasing the average population density. The spirals persist until $\omega \sim 0.075$, where they are overrun by wave trains nucleated from the interstices between the spirals (Fig. 3*E*), close and approaching ω_{SN}. These wave trains initially have a wavenumber larger than that of the spirals, but as ω increases further, their wave number decreases again due to the destruction of peaks.

In 1D systems, the destruction of peaks occurs when a plane wave crosses the right Busse-Balloon border (right limit of the green dashed region in Fig. 2*D*). Peak destruction is followed by a reorganization of the remaining peaks, converging to a wave train with a wavelength again inside the Busse Balloon (2, 5). This process maintains the system in stable wave train states while increasing ω until the last traveling pulse decays at the SNTP point. Similar mechanisms have been found in steady vegetation patterns and wave trains in systems with advection (3, 5, 56). The progressive destruction of peaks far beyond the tipping point of the homogeneous system, increasing the wavelength of wave trains in a 1D system is shown in *SI Appendix*, Fig. S3.

In 2D systems, where vegetation stripes are finite, a shrinking of the stripes from their tips is observed for large mortality values. This is the principal peak destruction mechanism observed in the simulation shown in Fig. 3 (Movie S7). This transition occurs for mortality values close but below ω_{SNTP}. No transverse destabilizing effects have been observed in this model, as the wave trains are stable in the transverse direction (see stability analysis of wave trains in *SI Appendix*, Text).

Traveling pulses, forming an isolated traveling stripe, are the ultimate resilient structures before extinction at ω_{SNTP}.

4. Discussion and Conclusions

We have proposed a simple model that, by including positive feedback and negative feedback mediated by toxins with a time scale similar to the characteristic population dynamics, is able to reproduce a variety of spatiotemporal dynamical regimes observed in different ecological contexts and the regime shifts among them. Without the toxin mediation, the system can show a strong Allee effect and the existence of the populated solution ends at a tipping point when increasing the natural mortality. By also considering noninstantaneous dynamics in the negative feedback, the system can exhibit excitable behavior, where initial homogeneous plant populations grow driven by a strong Allee effect, but eventually decay and die due to the toxin accumulation. In this case, the ecological tipping point occurs for mortalities below this excitable regime. However, in spatially extended systems, self-organized moving structures like wave trains and traveling pulses can persist even at mortality levels beyond the tipping point for homogeneous populations. The low toxin concentration at the leading edge of moving spatial structures enables plant growth through positive feedback. Behind these structures, however, toxins accumulate, causing a decline in population density. This self-organizing dynamic allows positive feedback to outweigh the negative impact of toxins in certain regions, thereby enhancing the system's resilience. These resilient traveling structures contrast with previous studies, where resilience was attributed to steady states (68) or steady spatial patterns (1, 2).

We performed a long simulation with a gradual increase in mortality in a 2D system and observed a progressive transition from homogeneous meadows to extinction going through turbulent regimes, spirals, wave trains, and traveling pulses in this precise order. This scenario is compatible with aerial images of *P. oceanica* meadows (Fig. 1 *A*–*D*), where there is theoretical and empirical evidence of positive and negative feedback, and of the role of plant–soil interactions in the formation of rings (6, 7, 33). According to our results, the mortality rates of the meadow in each area could be inferred from the aerial images. However, this inference assumes that the underlying parameters, including α and τ, remain consistent across the regions analyzed. However, the sequence of dynamical regimes observed when increasing ω is robust to parameter variations, as shown by the phase diagram in the parameter space (ω, α) (*SI Appendix*, Fig. S8).

The mean biomass density of spatiotemporal solutions is greater than that of homogeneous systems for the same mortality rate. Furthermore, these spatiotemporal solutions extend and survive far beyond the tipping points of the homogeneous vegetation cover.

In this article, we highlight the role of positive feedback in the formation of spatiotemporal structures in vegetation systems. The excitable medium that the ecosystem forms is related to local type-I excitability and the presence of a T-point (60, 63, 64). The bifurcations responsible for creating and stabilizing the excitable pulses, the *SL* and the T-point respectively, need a bistable regime and oscillations in the local (homogeneous) model, only possible if the model presents positive feedback. Similarly, other systems with positive feedback in addition to mediated negative feedback also show excitable regimes (7–9, 39, 40, 42, 43, 45).[†] Nevertheless, the role of positive feedback in the formation of these regimes is not discussed in these studies.

Models that do not include positive feedback show a very different pulse-like solution (10, 38, 41, 44). These pulse-like solutions are fronts of a stable populated solution propagating on the (unstable) bare soil state. These fronts exist only in parameter regions where the populated solution is stable and therefore do not give any spatiotemporal-induced resilience to the system. Furthermore, the system cannot be re-excited after one of these fronts has passed. Therefore, models without positive feedback cannot reproduce the formation of wave trains, spiral patterns, or empty rings.

Inhomogeneities and heterogeneous conditions can influence self-organization processes in vegetation systems (69) and can enhance resilience in large ecosystems (2). In excitable media, heterogeneous conditions can promote the formation of spirals and target patterns (70) or even induce a transition to a different dynamical regime (71). Studies applying heterogeneous backgrounds to plant-toxin models show deformations in the rings and the spontaneous generation of new vegetation patches, aligning more closely with observations in the real world (7). Furthermore, real *P. oceanica* meadows are typically geographically confined to regions with suitable environmental conditions. In practice, traveling structures that do not self-replicate and move in a single direction (e.g., wave trains and traveling pulses or expanding rings) will eventually reach the boundaries of the habitat and decay. These structures can thus be considered resilient but transient structures (72).

Finally, several experimental approaches could be used to test the hypotheses outlined in this paper. For example, adding iron to the rear of existing traveling pulses to inhibit the negative effects of sulfides (34, 36, 37) would stop plant recession widening the pulse. In addition, measuring growth and mortality rates at different locations of complex patterns would validate the mechanisms described in this work. This has been done partially

[†]In refs. 39, 40, and 43 the positive feedback is not introduced explicitly, but through nonlinearities in water consumption.

with traveling pulses (7), but not in more complicated structures such as spirals and turbulence. Finally, for restoration efforts in regions with known traveling structures, it would be advisable to consider the dynamics described in this work to decide where to transplant new shoots.

5. Materials and Methods

Spatiotemporal simulations were performed using the Julia package FourierFlows (73). We used a Pseudospectral Runge–Kutta 4 method with a complete time step $dt = 0.05$ (74). The simulations shown in Fig. 1 *E* and *G*, and in Fig. 3 were carried out on a grid with 2,048 × 2,048 grid points and a lateral size $L_x = L_y = 500$. The simulation in Fig. 1*F* was performed on a 1,200 × 1,200 grid with lateral size $L_x = L_y = 300$. The simulation in Fig. 1*H* was run on a 1,024 × 1,024 grid with lateral size $L_x = L_y = 250$. The simulations shown in Fig. 1 *E* and *G*, and in Fig. 3 were initialized near the state S_+, with mortality increased in steps of $\Delta\omega = 0.0016$ every $\Delta t = 200$. To prevent possible metastable structures, uncorrelated spatial Gaussian noise with a variance of $\sigma = 0.004$ was added to both the plant and toxin densities after each parameter change. The simulation shown in Fig. 1*F* was initialized with a radial Gaussian distribution of plants and toxins with amplitude $A = 0.7$ and variance $\sigma = 17.5$. These two initial distributions were displaced in space by $\Delta r = 2.8$ to break the radial symmetry. The simulation shown in Fig. 1*H* is initialized with a radial Gaussian distribution of plants and toxins with amplitude $A = 0.2$ and variance $\sigma = 25$.

Continuation of wave trains was performed using Keller's pseudo-arclength method (75–77). For wave trains with wavenumbers $k < 0.21$ we used a spatial step $dx = 0.1$. For those with $k > 0.21$, we used a smaller spatial step, $dx = 0.05$, to better control wavenumber selection. Stability computations have been performed using the same spatial discretization, using the method discussed in *SI Appendix*.

Data, Materials, and Software Availability. All study data are included in the article and/or supporting information.

ACKNOWLEDGMENTS. P.M.-S. and D.G. acknowledge financial support from project CYCLE (PID2021-123723OB-C22) funded by MCIN/AEI/10.13039/501100011033 and the European Regional Development Fund (ERDF) "A way of making Europe," the María de Maeztu project CEX2021-001164-M funded by the MCIN/AEI/10.13039/501100011033, and the European Union's Horizon's 2020 research and innovation programme (Grant agreement ID: 101093910, Ocean Citizen). P.M.-S. acknowledges support from the PhD contract (RTI2018-095441-B-C22) of the Spanish Ministry of Science and Innovation. The research of M.R. is supported by the European Research Council (ERC-Synergy project RESILIENCE, proposal no. 101071417) and by the Dutch Research Council (Netherlands Organization of Scientific Research, "Resilience in complex systems through adaptive spatial pattern formation," project no. OCENW.M20.169). We acknowledge helpful discussions with Robbin Bastiaansen, Tjisse van der Heide, and Elvira Mayol Alcover.

1. R. Lefever, O. Lejeune, On the origin of tiger bush. *Bull. Math. Biol.* **59**, 263–294 (1997).
2. M. Rietkerk *et al*., Evasion of tipping in complex systems through spatial pattern formation. *Science* **374**, eabj0359 (2021).
3. E. Siero *et al*., Striped pattern selection by advective reaction-diffusion systems: Resilience of banded vegetation on slopes. *Chaos* **25**, 036411 (2015).
4. R. Bastiaansen *et al*., Multistability of model and real dryland ecosystems through spatial self-organization. *Proc. Natl. Acad. Sci. U.S.A.* **115**, 11256–11261 (2018).
5. R. Bastiaansen, A. Doelman, M. B. Eppinga, M. Rietkerk, The effect of climate change on the resilience of ecosystems with adaptive spatial pattern formation. *Ecol. Lett.* **23**, 414–429 (2020).
6. J. Borum *et al*., Eelgrass fairy rings: Sulfide as inhibiting agent. *Mar. Biol.* **161**, 351–358 (2013).
7. D. Ruiz-Reynés *et al*., Self-organized sulfide-driven traveling pulses shape seagrass meadows. *Proc. Natl. Acad. Sci. U.S.A.* **120**, e2216024120 (2023).
8. N. Karst, D. Dralle, S. Thompson, Spiral and rotor patterns produced by fairy ring fungi. *PLoS One* **11**, e0149254 (2016).
9. C. Fernandez-Oto, D. Escaff, J. Cisternas, Spiral vegetation patterns in high-altitude wetlands. *Ecol. Complex.* **37**, 38–46 (2019).
10. L. X. Zhao *et al*., Fairy circles reveal the resilience of self-organized salt marshes. *Sci. Adv.* **7**, eabe1100 (2021).
11. E. Meron, Pattern formation in excitable media. *Phys. Rep.* **218**, 1–66 (1992).
12. A. S. Mikhailov, *Foundations of Synergetics I* (Springer, Berlin Heidelberg, 1994).
13. R. Kapral, K. Showalter, *Chemical Waves and Patterns* (Springer, Netherlands, 1995).
14. S. Alonso, M. Bär, B. Echebarria, Nonlinear physics of electrical wave propagation in the heart: A review. *Rep. Prog. Phys.* **79**, 096601 (2016).
15. R. Follmann, E. Rosa, W. Stein, Dynamics of signal propagation and collision in axons. *Phys. Rev. E* **92**, 032707 (2015).
16. M. Dahlem, S. Müller, Reaction-diffusion waves in neuronal tissue and the window of cortical excitability. *Ann. Phys.* **516**, 442–449 (2004).
17. W. J. Rappel, The physics of heart rhythm disorders. *Phys. Rep.* **978**, 1–45 (2022).
18. K. J. Lee, W. McCormick, J. Pearson, H. L. Swinney, Experimental observation of self-replicating spots in a reaction-diffusion system. *Nature* **369**, 215–218 (1994).
19. F. Marino, S. Balle, Excitable optical waves in semiconductor microcavities. *Phys. Rev. Lett.* **94**, 094101 (2005).
20. D. Gomila, M. A. Matías, P. Colet, Excitability mediated by localized structures in a dissipative nonlinear optical cavity. *Phys. Rev. Lett.* **94**, 063905 (2005).
21. Y. Herooty, P. Bar, H. Yizhaq, O. Katz, Soil hydraulic properties and water source-sink relations affect plant rings' formation and sizes under arid conditions. *Flora* **270**, 151664 (2020).
22. E. Sheffer, H. Yizhaq, E. Gilad, M. Shachak, E. Meron, Why do plants in resource-deprived environments form rings? *Ecol. Complex.* **4**, 192–200 (2007).
23. E. Sheffer, H. Yizhaq, M. Shachak, E. Meron, Mechanisms of vegetation-ring formation in water-limited systems. *J. Theor. Biol.* **273**, 138–146 (2011).
24. E. Meron, *Nonlinear Physics of Ecosystems* (CRC Press, 2015).
25. S. Ravi, P. D'Odorico, L. Wang, S. Collins, Form and function of grass ring patterns in arid grasslands: The role of abiotic controls. *Oecologia* **158**, 545–555 (2008).
26. N. Adachi, I. Terashima, M. Takahashi, Central die-back of monoclonal stands of *Reynoutria japonica* in an early stage of primary succession on mount fuji. *Ann. Bot.* **77**, 477–486 (1996).
27. J. McAuliffe, E. Hamerlynck, M. Eppes, Landscape dynamics fostering the development and persistence of long-lived creosotebush (*Larrea tridentata*) clones in the Mojave desert. *J. Arid Environ.* **69**, 96–126 (2007).
28. G. Bonanomi *et al*., Ring formation in clonal plants. *Commun. Ecol.* **15**, 77–86 (2014).
29. L. Carlton, N. C. Duncritts, Y. A. Chung, J. A. Rudgers, Plant-microbe interactions as a cause of ring formation in *Bouteloua gracilis*. *J. Arid Environ.* **152**, 1–5 (2018).
30. Inderjit, R. M. Callaway, E. Meron, Belowground feedbacks as drivers of spatial self-organization and community assembly. *Phys. Life Rev.* **38**, 1–24 (2021).
31. M. B. Eppinga, W. H. V. der Putten, J. D. Bever, Plant-soil feedback as a driver of spatial structure in ecosystems a commentary on "Belowground feedbacks as drivers of spatial self-organization and community assembly" by Inderjit, Ragan M. Callaway and Ehud Meron. *Phys. Life Rev.* **40**, 6–14 (2022).
32. M. Bonacorsi, C. Pergent-Martini, N. Breand, G. Pergent, Is *Posidonia oceanica* regression a general feature in the mediterranean sea? *Mediterr. Mar. Sci.* **14**, 193–203 (2013).
33. P. S. Maxwell *et al*., The fundamental role of ecological feedback mechanisms for the adaptive management of seagrass ecosystems–A review. *Biol. Rev.* **92**, 1521–1538 (2017).
34. M. Holmer, C. M. Duarte, N. Marbà, Iron additions reduce sulfate reduction rates and improve seagrass growth on organic-enriched carbonate sediments. *Ecosystems* **8**, 721–730 (2005).
35. M. L. Calleja, N. Marbà, C. M. Duarte, The relationship between seagrass (*Posidonia oceanica*) decline and sulfide porewater concentration in carbonate sediments. *Estuar. Coast. Shelf Sci.* **73**, 583–588 (2007).
36. N. Marbà *et al*., Iron additions reduce sulfide intrusion and reverse seagrass (*Posidonia oceanica*) decline in carbonate sediments. *Ecosystems* **10**, 745–756 (2007).
37. N. Marbà *et al*., Sedimentary iron inputs stimulate seagrass (*Posidonia oceanica*) population growth in carbonate sediments. *Estuar. Coast. Shelf Sci.* **76**, 710–713 (2008).
38. F. Cartenì *et al*., Negative plant soil feedback explaining ring formation in clonal plants. *J. Theor. Biol.* **313**, 153–161 (2012).
39. A. Marasco *et al*., Vegetation pattern formation due to interactions between water availability and toxicity in plant-soil feedback. *Bull. Math. Biol.* **76**, 2866–2883 (2014).
40. A. Iuorio, F. Veerman, The influence of autotoxicity on the dynamics of vegetation spots. *Phys. D Nonlinear Phenom.* **427**, 133015 (2021).
41. A. Iuorio, N. Salvatori, G. Toraldo, F. Giannino, Analysis and numerical simulations of travelling waves due to plant-soil negative feedback. *Eur. J. Appl. Math.* **35**, 554–565 (2023).
42. G. Grifò, A. Iuorio, F. Veerman, Far-from-equilibrium traveling pulses in sloped semiarid environments driven by autotoxicity effects. *SIAM J. Appl. Math.* **85**, 188–209 (2025).
43. P. Carter, A. Doelman, A. Iuorio, F. Veerman, Travelling pulses on three spatial scales in a Klausmeier-type vegetation-autotoxicity model. *Nonlinearity* **37**, 095008 (2024).
44. N. Salvatori *et al*., Process based modelling of plants-fungus interactions explains fairy ring types and dynamics. *Sci. Rep.* **13**, 19918 (2023).
45. F. A. Davidson, B. D. Sleeman, A. D. M. Rayner, J. W. Crawford, K. Ritz, Travelling waves and pattern formation in a model for fungal development. *J. Math. Biol* **35**, 589–608 (1997).
46. T. Bohr, A. W. Pedersen, M. H. Jensen, Transition to turbulence in a discrete Ginzburg-Landau model. *Phys. Rev. A* **42**, 3626–3629 (1990).
47. H. Chaté, P. Manneville, Phase diagram of the two-dimensional complex Ginzburg-Landau equation. *Phys. A Stat. Mech. Appl.* **224**, 348–368 (1996).
48. M. M. van Katwijk *et al*., Global analysis of seagrass restoration: The importance of large-scale planting. *J. Appl. Ecol.* **53**, 567–578 (2015).
49. E. Mayol *et al*., Understanding the depth limit of the seagrass *Cymodocea nodosa* as a critical transition: Field and modeling evidence. *Mar. Environ. Res.* **182**, 105765 (2022).
50. T. van der Heide *et al*., Positive feedbacks in seagrass ecosystems: Implications for success in conservation and restoration. *Ecosystems* **10**, 1311–1322 (2007).
51. T. van der Heide *et al*., Toxicity of reduced nitrogen in eelgrass (*Zostera marina*) is highly dependent on shoot density and pH. *Oecologia* **158**, 411–419 (2008).
52. J. Carr, P. D'Odorico, K. McGlathery, P. Wiberg, Stability and bistability of seagrass ecosystems in shallow coastal lagoons: Role of feedbacks with sediment resuspension and light attenuation. *J. Geophys. Res. Biogeosci.* **115**, G03011 (2010).

53. J. Carr, P. D'Odorico, K. McGlathery, P. Wiberg, Modeling the effects of climate change on eelgrass stability and resilience: Future scenarios and leading indicators of collapse. *Mar. Ecol. Prog. Ser.* **448**, 289–301 (2012).
54. M. L. Rosenzweig, Paradox of enrichment: Destabilization of exploitation ecosystems in ecological time. *Science* **171**, 385–387 (1971).
55. I. S. Aranson, L. Kramer, The world of the complex Ginzburg-Landau equation. *Rev. Mod. Phys.* **74**, 99–143 (2002).
56. K. Siteur *et al.*, Beyond turing: The response of patterned ecosystems to environmental change. *Ecol. Complex.* **20**, 81–96 (2014).
57. M. Bär *et al.*, Chemical turbulence and standing waves in a surface reaction model: The influence of global coupling and wave instabilities. *Chaos Interdiscip. J. Nonlinear Sci.* **4**, 499–508 (1994).
58. H. Chaté, P. Manneville, Transition to turbulence via spatio-temporal intermittency. *Phys. Rev. Lett.* **58**, 112–115 (1987).
59. Q. Ouyang, J. M. Flesselles, Transition from spirals to defect turbulence driven by a convective instability. *Nature* **379**, 143–146 (1996).
60. P. Moreno-Spiegelberg, A. Arinyo-i Prats, D. Ruiz-Reynés, M. A. Matias, D. Gomila, Bifurcation structure of traveling pulses in type-I excitable media. *Phys. Rev. E* **106**, 034206 (2022).
61. S. Nii, The accumulation of eigenvalues in a stability problem. *Phys. D Nonlinear Phenom.* **142**, 70–86 (2000).
62. B. Sandstede, A. Scheel, Gluing unstable fronts and backs together can produce stable pulses. *Nonlinearity* **13**, 1465–1482 (2000).
63. M. Or-Guil, J. Krishnan, I. G. Kevrekidis, M. Bär, Pulse bifurcations and instabilities in an excitable medium: Computations in finite ring domains. *Phys. Rev. E* **64**, 046212 (2001).
64. A. Arinyo-i Prats, P. Moreno-Spiegelberg, M. A. Matias, D. Gomila, Traveling pulses in type-I excitable media. *Phys. Rev. E* **104**, L052203 (2021).
65. E. Díaz-Almela, N. Marbà, R. Martínez, R. Santiago, C. M. Duarte, Seasonal dynamics of *Posidonia oceanica* in Magalluf Bay (Mallorca, Spain): Temperature effects on seagrass mortality. *Limnol. Oceanogr.* **54**, 2170–2182 (2009).
66. N. Marbà, C. M. Duarte, Mediterranean warming triggers seagrass (*Posidonia oceanica*) shoot mortality. *Glob. Chang. Biol.* **16**, 2366–2375 (2010).
67. I. Savva, S. Bennett, G. Roca, G. Jordà, N. Marbà, Thermal tolerance of mediterranean marine macrophytes: Vulnerability to global warming. *Ecol. Evol.* **8**, 12032–12043 (2018).
68. C. S. Holling, Resilience and stability of ecological systems. *Annu. Rev. Ecol. Syst.* **4**, 1–23 (1973).
69. S. Echeverría-Alar, D. Pinto-Ramos, M. Tlidi, M. G. Clerc, Effect of heterogeneous environmental conditions on labyrinthine vegetation patterns. *Phys. Rev. E* **107**, 054219 (2023).
70. J. Maselko, K. Showalter, Chemical waves in inhomogeneous excitable media. *Phys. D Nonlinear Phenom.* **49**, 21–32 (1991).
71. M. Dix, T. Lilienkamp, S. Luther, U. Parlitz, Influence of conduction heterogeneities on transient spatiotemporal chaos in cardiac excitable media. *Phys. Rev. E* **110**, 044207 (2024).
72. A. Hastings *et al.*, Transient phenomena in ecology. *Science* **361**, eaat6412 (2018).
73. N. C. Constantinou *et al.*, FourierFlows/FourierFlows.jl: v0.10.5. Zenodo. https://zenodo.org/doi/10.5281/zenodo.1161724. Accessed 15 January 2024.
74. R. Toral, P. Colet, *Stochastic Numerical Methods: An Introduction for Students and Scientists* (Wiley-VCH, 2014).
75. W. C. Rheinboldt, Lectures on numerical methods in bifurcation problems (Herbert B. Kelley). *SIAM Rev.* **30**, 677–677 (1988).
76. H. D. Mittelmann, A pseudo-arclength continuation method for nonlinear eigenvalue problems. *SIAM J. Numer. Anal.* **23**, 1007–1016 (1986).
77. T. F. C. Chan, H. B. Keller, Arc-length continuation and multigrid techniques for nonlinear elliptic eigenvalue problems. *SIAM J. Sci. Stat. Comput.* **3**, 173–194 (1982).